Transient Three-Dimensional Analysis of Side Load in Liquid Rocket Engine Nozzles

Ten-See Wang*
NASA Marshall Space Flight Center, Huntsville, Alabama, 35812

Three-dimensional numerical investigations on the nozzle start-up side load physics were performed. The objective of this study is to identify the three-dimensional side load physics and to compute the associated aerodynamic side load using an anchored computational methodology. The computational methodology is based on an unstructured-grid, and pressure-based computational fluid dynamics formulation, and a simulated inlet condition based on a system calculation. Finite-rate chemistry was used throughout the study so that combustion effect is always included, and the effect of wall cooling on side load physics is studied. The side load physics captured include the afterburning wave, transition from free-shock to restricted-shock separation, and lip Lambda shock oscillation. With the adiabatic nozzle, free-shock separation reappears after the transition from free-shock separation to restricted-shock separation, and the subsequent flow pattern of the simultaneous free-shock and restricted-shock separations creates a very asymmetric Mach disk flow. With the cooled nozzle, the more symmetric restricted-shock separation persisted throughout the start-up transient after the transition, leading to an overall lower side load than that of the adiabatic nozzle. The tepee structures corresponding to the maximum side load were addressed.

I. Introduction

Nozzle side loads are potentially detrimental to the integrity and life of almost all launch vehicle nozzles. For example, side load problems have been found for J2 engine[1], Space Shuttle Main Engine (SSME) Block I, and recently, the Fastrac Engine nozzles. Most recently, the European Vulcain engine nozzle[2] and the Japanese LE-7A engine nozzle[3] have also experienced side load difficulties. Unfortunately, the current level of understanding of the cause of nozzle side loads is limited and does not allow the accurate prediction of side load severity for new nozzle designs. The lack of a detailed prediction capability results in reduced life and increased weight for reusable nozzle systems. Simple models exist to predict side load magnitudes but are overly conservative and not fully validated. A clear understanding of the mechanisms and factors that contribute to side loads during engine startup, shutdown, and steady-state operations must be attained. Subsequently, a predictive tool based on computational fluid dynamics (CFD) must be developed to aid the development of future reusable engines.

Wang[4] reported the first attempt in using CFD to study the separated flows inside an axisymmetric SSME nozzle, using scheduled start-up and shut-down sequences. Chen, et al.[5] reported a similar effort on an axisymmetric cold flow J2S nozzle later, using impulsive starts and cut-offs. Both captured the nozzle hysteresis phenomenon that is considered to be one of the basic characteristics of liquid rocket engine nozzles, and both fell short of predicting asymmetric flows due to the symmetric boundary condition limitation. Yonezawa, et al.[6] made the first two-dimensional (2-D) nozzle side load prediction for the Japanese LE-7A engine. Yonezawa, et al.[7] then made the first 3-D side load prediction for the LE-7, LE-7A and CTP50-R5-L nozzles. They computed free-shock separation (FSS) and small side load for the LE-7, simultaneous occurrence of FSS and restricted-shock separation (RSS) and medium side load for LE-7A, and transition from FSS to RSS and high side load caused by RSS for the CTP50-R5-L nozzles. The works of Yonezawa, et al[6,7] however, ignored the effect of combustion of the excess fuel and assumed a linear ramp profile. In addition, the authors stated that the grid used was probably too coarse, resulting in overestimated flow fluctuation, smearing of distinctive peaks, and inadequate shape of the Mach disk.

After the works of Yonezawa, et al[6,7], Wang[8] performed a series of 2-D and axisymmetric numerical studies on the SSME nozzle start-up side load physics, using hybrid grids that were anchored for axial force and wall heat fluxes.[9] The side load physics captured in that study include the Coanda effect, afterburning wave, transition from FSS to RSS and vice versa, and lip Lambda shock oscillation. More importantly, it is found that inlet ramp rate

* Staff Consultant, Applied Fluid Dynamics Analysis Group, TD64, Senior Member AIAA.

determines the thruster filling, and combustion decides the distribution of thermo-chemical properties in the propulsive flow; as such, both affect the formation and duration of the asymmetric flow that lead to the side forces. The lesson learned from that study[8] sets up the computational strategy for the three-dimensional investigation of the SSME nozzle side load physics in this study. That is, the computational methodology is based on an unstructured-grid computational fluid dynamics (CFD) formulation, and a simulated inlet history. And the finite-rate chemistry is turned on throughout the study in order to capture the afterburning that determines the proper thermo-chemical property distribution. In addition, the effect of (regenerative) wall cooling is investigated as a potential design strategy for side load reduction.

II. Computational Methodology

Computational Fluid Dynamics

The CFD methodology is based on a multi-dimensional, finite-volume, viscous, chemically reacting, unstructured grid, and pressure-based formulation. Time-varying transport equations of continuity, momentum, global energy (total enthalpy), turbulence, and species continuity were employed. A predictor and corrector solution algorithm was employed to provide coupling of the governing equations. A second-order central-difference scheme was employed to discretize the diffusion fluxes and source terms of the governing equations. For the convective terms, a second-order upwind total variation diminishing difference scheme was used. To enhance the temporal accuracy, a second-order backward difference scheme was employed to discretize the temporal terms. Details of the numerical algorithm can be found in Ref's 9-12.

An extended k-ε turbulence model[13] was used to describe the turbulence. A modified wall function approach was employed to provide wall boundary layer solutions that are less sensitive to the near-wall grid spacing. Consequently, the model has combined the advantages of both the integrated-to-the-wall approach and the conventional law-of-the-wall approach by incorporating a complete velocity profile and a universal temperature profile[14]. A 7-species, 9-reaction detailed mechanism[14] was used to describe the finite-rate, hydrogen/oxygen (H_2/O_2) afterburning chemical kinetics. The seven species are H_2, O_2, H_2O, O, H, OH, and N_2.

Simulated Start-up Sequence

The thruster inlet properties were obtained from an engine system calculation, simulating the valve sequence. Figure 1 shows some of the inlet flow properties: the time-varying inlet pressure, temperature, and equivalence ratio profiles. And it is hereby referred to as the nominal 5 s start-up sequence, in order to differentiate with the shortened sequence in the ramp rate study. It can be seen that there are two significant pressure rise events. The first one occurs at 1.5 s due to oxygen prime, while the second one occurs at about 2.4 s, caused by the step opening of the oxygen in the pre-burners. It can be seen that the thruster environment is fuel rich throughout the start-up transient, setting up the potential for afterburning. The high equivalence ratio in the first 0.2 s is not significant since the flow rate is negligible.

III. Computational Grid Generation

Parametric studies conducted[9] show that a structured-cell dominated hybrid mesh 3d6 performed more favorably than an unstructured-cell dominated hybrid mesh (3d9) both in accuracy and efficiency, on flow physics and prediction of nozzle design parameters such as axial force and heat fluxes. Assuming that a grid suitable for axial force calculation is sufficient for side force calculation, grid 3d6 was used in this study and its layout is shown in Fig. 2. It can be seen that structured (hexahedral) cells are used in the thruster and plume region, while unstructured (prismatic) elements are used in the freestream region. It was generated using a software package GRIDGEN.[15] The total number of points is 1,286,934, comparing to the 145,500, 145,500, and 405,900 points used on LE-7, LE-7A, and CTP50-R5-L,[7] respectively.

IV. Boundary and Inlet Conditions

Fixed total condition was used for the outer boundary and a total pressure of 1 atm was used to simulate the nozzle hot-firing at sea level. No-slip condition was specified for the solid walls. The inlet flow properties obtained from the system simulation include the time varying total pressure, temperature, and propellant composition. The time varying propellant composition was preprocessed with the Chemical Equilibrium Calculation program[16],

assuming the propellants were ignited to reach equilibrium composition immediately at the injector faceplate. The fuel rich environment indicates the inlet composition contains mostly steam and excess hydrogen.

V. Results and Discussion

The computations were performed on several cluster machines using 22~32 processors. For the nominal 5 s start-up sequence, global time steps of 10 μs were used in the beginning, reduced to 2.5 μs in the afterburning wave event, increased to 5 μs the rest of the way. For the impulsive start, 1 μs was used throughout the computation. The adiabatic wall case was computed first; as the elapsed time reached 1.5 s, the (regeneratively) cooled wall case was started in parallel by specifying a cooled wall temperature distribution[9], to simulate the effect of heat loss due to the cooling process. The cooled wall temperature was not applied in the beginning because the injection temperature was much colder. This procedure implies the flow processes were identical for the two cases prior to 1.5 s. The computed side forces for the adiabatic and cooled wall cases from 0 ~ 2 s are shown in Fig's 3 and 4, respectively. Note that the first pressure rise event occurs after 1.5 s. From Fig's 3 and 4, it can be seen that the overall computed side load for the adiabatic nozzle is higher than that of the cooled nozzle; the reasons for which will be discussed after the computed flow physics are delineated.

As indicated in Fig. 1, the pressure rises rather slowly, after the start command. Yet the chamber gradually fills up and a detached jet emerges from the throat at around 0.175 s. Unlike the Coanda effect[17] captured in the low aspect-ratio, 2-D planar nozzle,[8] with which the core jet and subsequent Mach disk flow adhere to the wall, creating asymmetric flow and producing early side forces; the three-dimensional core jet is fairly centered, however, and produces negligible side forces during the core jet flow period. As a result, even as the Mach disk flow develops after 1.2 s and some small side load appears between 1.2 and 1.5 s, the flow is still fairly centered. It is speculated that the geometrical volume available for air pumping between the core jet and the wall is much larger in a 3-D nozzle than that of a 2-D nozzle, hence the difference. The side load produced in that period is believed to be caused by the oscillation of the supersonic jets of the Mach disk flow, which is in a FSS mode since the supersonic jets are oscillating freely but away from the wall. As time goes on, the magnitude of the oscillation increases because the mass flow increases.

At 1.5 s into the start-up transient, the composition of the Mach disk flow is essentially hydrogen-rich steam. That leads to afterburning in the mixing layer between the supersonic jet and the ambient air, raising temperature, as shown in the temperature contours at 1.503 s in Fig. 5. That elevated temperature front quickly spreads through the mixing layer, creating a fast expanding hot gas that glows, much like that observed in the hot-fire test, as indicated in the rest of the plots in Fig. 5. The combustion wave starts at the mixing layer inside the nozzle and propagates in all directions. A portion of the combustion wave moving in the transversal direction would hit the wall, generating the first significant side load (Fig. 3 and Fig. 4) and several smaller ones thereafter due to the shock reflections, while the rest expands away, as depicted in the pressure and Mach number contours shown in Fig. 6 and Fig. 7. In the mean time, the hydrogen jet is being consumed away, as shown in the hydrogen mass fraction contours in Fig. 8: the initial afterburning of hydrogen in the mixing layer at 1.503 s; the reduction of the hydrogen to a "waist" like jet at 1.504 s; the disappearance of the "waist" at 1.505 s; and a much shorter hydrogen jet at 1.506 s. Since this afterburning wave happens in both adiabatic and cooled nozzle cases, only the contours for the cooled nozzle are shown. Note that the disk of the Mach disk flow appears to retreat with the shortening hydrogen jet.

Soon after the effect of the afterburning wave is gone, the apparent "depleted" hydrogen jet is gradually filled up due to the continuous replenishment from the chamber, and the free-shock separated Mach disk flow propagates again. Since the afterburning continues in the mixing layer, adding instability to the already unstable supersonic jet, the Mach disk itself is oscillating back and forth, not only responding to the oscillating supersonic jets, but also responding to all the changes in the nozzle contour and the upstream boundary conditions. For the cooled nozzle, Fig. 9 shows a typical oscillating, free-shock separated Mach disk flow at 1.515 s. That is, the supersonic jet stemming from the Mach disk does not touch the wall. At 1.520 s, however, the upstream portion of the supersonic jet is moving towards the wall – an obvious transition stage due to the Coanda effect.[8,17] At 1.525 s, the supersonic jet completely adheres to the wall, enclosing a recirculation region, resulting in a distinctive RSS pattern. At 1.530 s, the restricted shock pattern persists, except the disk retreats upstream. The RSS flow pattern persists thereafter. The transition from FSS to RSS creates the second significant side load (Fig. 4, as well as in Fig. 3). The oscillation of the restricted shock, or restricted-shock oscillation, also creates side load, demonstrated by the asymmetric supersonic jet (and flow recirculation) pattern at 1.530 s. When ramp rate slows, the RSS caused side load also decreases (Fig. 4).

For the adiabatic nozzle, FSS-to-RSS also occurs at 1.520 s, and RSS occurs from 1.521 to 1.523 s. After which RSS-to-FSS occurs at 1.524 s and it is FSS thereafter at 1.525 s. Hence, the computed side load physics for the adiabatic nozzle is distinctively different from those of the cooled nozzle. That is, after the FSS-to-RSS transition, the RSS reverts back to the FSS for the adiabatic nozzle and stays that way for a long time, while the RSS persists all the way for the cooled nozzle. Note that previous effort[8] on the adiabatic, axisymmetric nozzle, showed FSS-to-RSS at around 1.525 s, turned to FSS at 1.550 s, and then became RSS again at 1.600 s and stays with RSS thereafter. These differences indicate that the separation flow pattern after the FSS-to-RSS transition is sensitive and unstable. And it is speculated that axisymmetric calculation allows only axial and radial changes and not in the tangential direction, hence a forced conversion to RSS at the third transition, while the 3-D calculation allows changes in all three dimensions, therefore the transition depends on factors such as the boundary conditions. On the other hand, for the adiabatic nozzle using impulse start, RSS persists after the transition. Figure 10 shows the computed side forces for the adiabatic nozzle using impulse start, in which the transition of FSS-to-RSS occurs at about 0.005 s and stays at RSS until the Lambda leaves the lip at about 0.00825 s. Therefore, for 3-D nozzles, the transition from FSS to RSS depends not only on the boundary condition, but also on the ramp rate and equivalence ratio history.[8] Note that the side load (Fig. 3) due to FSS-to-RSS transition for the 5 s nominal start sequence is about 2.5 times that of the impulse start (Fig. 10). Furthermore, the side forces become negligible after 0.00825 s (Fig. 10).

With a cold wall, density is higher in the boundary layers of both the attached and recirculated regions. That leads to higher eddy viscosity, higher momentum, and thinner boundary layers; which in turn results in lower pressures in the boundary layers in the recirculated region and on the wall-side of the supersonic jet. Coanda effect then takes over which draws the supersonic jet to the wall, transiting a FSS to RSS. For an adiabatic wall where the temperature is close to stagnation temperature, the opposite is true. This cold wall affected flow separation physics agrees with those reported in Ref's 18 and 19 in which they found thinner, cold-wall boundary is less susceptible to separation than were the hot-wall results in steady nozzle flows. As a result, the computed side load (Fig. 3) of the adiabatic nozzle is in general much larger than that (Fig. 4) of the cooled nozzle. This is because not only the adiabatic nozzle flow is more energetic, the associated FSS flow pattern is less stable and more asymmetric than that of the RSS. The four jumps in side load (after 1.6 s) in Fig. 3 is associated with the in-as-many attempts trying to adhering to the wall by the Mach disk flow, creating quite an asymmetric flow pattern. Those attempts of wall-adhering are not successful until the chamber pressure reaches a high enough level (Fig. 11).

Figures 11 and 12 show the computed side loads for the adiabatic and cooled nozzles from 2 ~ 4 s, covering the second pressure rise event starting at 2.4 s. These computations were started using the solutions of 1.8 s which has a chamber pressure very close to that of the 2.4 s, in order to improve the turn-around time and avoid the unphysical blast wave often associated with an impulsive start. The pressure rises linearly and significantly from here to the eventual full-power level at about 4 s. It can be seen that the computed side loads are in general larger and more unstable than those after the first pressure rise event (Fig's 3 and 4), due to the significantly increased chamber pressure. For the adiabatic nozzle, as mentioned before, the supersonic jet associated with the FSS is not stable. It flops around and periodically adheres to one-side of the nozzle, creating simultaneous asymmetric FSS and RSS flow patterns, thereby generating jumps in side forces (Fig. 11). Figure 13 shows a snapshot of the FSS flow pattern and that of simultaneous FSS and RSS on y-plane and z-plane, respectively, at 2.625 s. Note that the Mach stem of the RSS is longer than that of the FSS in the contours of the z-plane, showing flow instability and asymmetry. When the separation line on the wall is plotted, the result is a slanted plane, as indicated in the OH concentration contours in Fig. 13. This slanted plane is very similar to the "tilted plane concept" described in Ref. 1, except the underlying physics computed in here is much more complicated because of the simultaneous FSS and RSS flow pattern. The "hot" region beneath the slanted plane is impressed by the recirculated region and part of the supersonic jet of the RSS flow pattern.

Figure 14 shows the RSS flow patterns for the cooled nozzle at 2.580 s. As indicated above, both the Mach disk and the supersonic jet are oscillating, generating side load (Fig. 12). It can be seen that the RSS side load of the cooled nozzle is lower than that of the co-existent FSS and RSS of the adiabatic nozzle, since RSS flow pattern is less asymmetric than that of the simultaneous FSS and RSS (Fig. 13). This can be seen from the almost symmetric wall OH concentration contours. The high OH concentration "band" represents the contact surface by the recirculated region which is bounded by the two stems of the Lambda shock, inside which is filled with hot, combustion products. Note the Mach disk on the y-plane slants to the right, while that on the z-plane slants to the left, indicating the unstable nature of the restricted-shock separated Mach disk flow.

The elapsed times computed so far for the adiabatic and cooled nozzle cases are indicated in Fig's 11 and 12, approaching or over 2.6 s, about 0.4 s short of the critical 3 s time when the separation plane can be noted as a series of intersecting conical lines or tepee structures. According to the test observations, a few tepee structures are just

becoming visible at 2.9 ~ 3 s; at this time the tepee structures appear to be few and isolated and are not characterized by the continuous saw-tooth pattern covering the full nozzle circumference as seen at higher chamber pressures. As chamber pressure continues to increase the number of visible tepee structures increases and the tepees begin to join together to form the characteristic saw-tooth pattern, at around 3.1 s, the approximate time when the maximum side load occurs. Although the computations have not reached the critical 3 s elapsed time, a preview of what is to come is shown in Fig. 15. This is accomplished by showing the results of the impulse start which took much less time (about 0.00825 s) for the Mach disk flow to reach nozzle lip. As seen in the Mach number contours of Fig. 15, the first stem of the Lambda shock has stepped out the lip while the second stem is still inside the lip. And an approximate saw-tooth tepee flow pattern can be seen from the wall OH concentration contours. As expected, the amplitude of the tepee in Fig. 15 is smaller than that of the test observation due to the impulsive start. It is anticipated that regular sized tepee structures will be captured and the corresponding maximum side load computed when the elapsed times of the computations reach the critical 3 s.

VI. Conclusions

Three-dimensional numerical investigations on the nozzle start-up side load physics and predictions of the associated aerodynamic side load for adiabatic and cooled nozzles were performed. The computational methodology is based on a multi-dimensional, finite-volume, viscous, chemically reacting, unstructured grid, and pressure-based computational fluid dynamics formulation, and a simulated inlet condition based on a system calculation. The side load physics captured include the afterburning wave, transition from FSS to RSS, and lip Lambda shock oscillation. The ramp rate, equivalence ratio, and wall boundary condition affect the side-load physics and the magnitude of the side load. With the adiabatic nozzle, FSS reappears after the transition from FSS to RSS, and the subsequent flow pattern of the simultaneous FSS and RSS creates a very asymmetric Mach disk flow. With the cooled nozzle, the more symmetric RSS persisted throughout the start-up transient after the transition, leading to an overall lower side load than that of the adiabatic nozzle. The tepee structures corresponding to the maximum side load were addressed.

Acknowledgments

This study was partially supported by a MSFC FY03 CDDF effort entitled "Nozzle Side Load Technology" of which Joe Ruf is the principal investigator who conducted experimental and simplified analytical investigations. The author wishes to thank Chief Aerodynamicist Werner Dahm for his guidance, and Y.-S. Chen of Engineering Sciences, Inc. for technical support and discussions. Also, James Beck of Rocketdyne Boeing provided valuable insight into SSME side load physics and suggested cooled wall computation. David Seymour provided the initial engine start-up information.

References

[1]Nave, L.H., and Coffey, G.A., "Sea Level Side Loads in High-Area-Ratio Rocket Engines," AIAA Paper 73-1284, Nov. 1973.

[2]Hageman, G., Alting, J., and Preclik, D., "Scalability for Rocket Nozzle Flows Based on Subscale and Full-Scale Testing," *Journal of Propulsion and Power*, Vol. 19, No. 3, 2003, pp.321-331.

[3]Wantabe, Y., Sakazume, N., and Tsuboi, M., "LE-7A Engine Nozzle Problems During the Transient Operations," AIAA Paper 2002-3841, July 2002.

[4]Wang, T.-S., "Numerical Study of the Transient Nozzle Flow Separation of Liquid Rocket Engines," *Computational Fluid Dynamics Journal*, Vol. 1, No. 3, Oct. 1992, pp. 319-328.

[5]Chen, C.L., Chakravathy, S.R., and Hung, C.M., "Numerical Investigation of Separated Flows," *AIAA Journal*, Vol. 32, No. 9, Sept. 1994, pp. 1836-1843.

[6]Yonezawa, K., Yokota, K., Watanabe, Y., Tsujimoto, K., and Abe, T., "2-D Numerical Simulation of Side Loads in Rocket Nozzles," Proceedings of 23rd International Symposium on Space Technology and Science, Japan Society for Aeronautical and Space Sciences, 2002, pp. 1146-1151.

[7]Yonezawa, K., Yokota, K., Tsujimoto, K., Sakazume, N., and Watanabe, Y., "Three-Dimensional Unsteady Flow Simulation of Compressed Truncated Perfect nozzles," AIAA Paper 2002-3991, July 2002.

[8]Wang, T.-S., "Transient Two-Dimensional Analysis of Side Load in Liquid Rocket Engine Nozzles," AIAA Paper 2004-3680, 11-14 July, 2004.

[9]Wang, T.-S., "Multidimensional Unstructured-Grid Liquid Rocket Engine Nozzle Performance and Heat Transfer Analysis," AIAA Paper 2004-4016, 11-14 July, 2004.

[10]Chen, Y.-S., Liu, J., Zhang, S., and Mallapragada, P., "An Integrated Tool for Launch Vehicle Base-Heating Analysis,"

Final Report, Engineering Sciences, Inc., Huntsville, AL, December 2001.

[11]Wang, T.-S., Chen, Y.-S., Liu, J., Myrabo, L.N., and Mead, F.B. Jr., "Advanced Performance Modeling of Experimental Laser Lightcraft," *Journal of Propulsion and Power,* Vol. 18, No. 6, November-December, 2002, pp. 1129-1138.

[12]Chen. Y.-S., Zhang S., and Liu, J., "Stage Separation Performance Analysis Project," Final Report, Engineering Sciences, Inc., Huntsville, AL, June, 2002.

[13]Chen, Y.-S., and Kim, S. W., "Computation of Turbulent Flows Using an Extended k-ε Turbulence Closure Model," NASA CR-179204, Oct. 1987.

[14]Wang, T.-S., Droege, A., D'Agostino, M., Lee, Y.-C., and Williams, R., "Base-Bleed Effect on X-33 Aerospike Plume Induced Base-Heating Environment During Power-Pack Out," AIAA Paper 2003-3651, June 2003.

[15]Steinbrenner, J.P., Chawner, J.R., and Fouts, C., "Multiple Block Grid Generation in the interactive Environment," AIAA Paper 90-1602, June 1990.

[16]Svehla, R.A., and McBride, B.J., "FORTRAN IV Computer Program for Calculation of Thermodynamic and Transport Properties of Complex Chemical Systems," NASA TN D-7056, Jan. 1973.

[17]Kumada, M., Mabuchi, I., and Oyakawa, K., "Studies on Heat Transfer to Turbulent Jets with Adjacent Boundaries," *Bulletin of the Japan Society of Mechanical Engineers*, Vol. 16, No. 100, 1973, pp. 1712-1722.

[18]Chang, C.L., Kronzon, Y., and Merkle, C.L., "Time-Iterative Solutions of Viscous Supersonic Nozzle Flows," *AIAA Journal*, Vol. 26, No. 10, 1988, pp. 1208-1215.

[19]Shimura K., Asako, Y., and Lee, J.H., "Numerical Analysis for Supersonic Flows in a Cooled Nozzle," *Numerical Heat Transfer*, Part A., Vol. 26, 1994, pp.631-641.

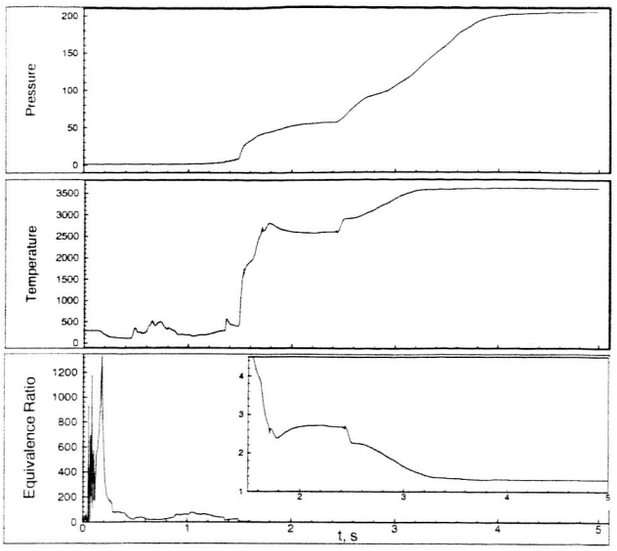

Fig. 1 Simulated thruster inlet properties during the start-up transient.

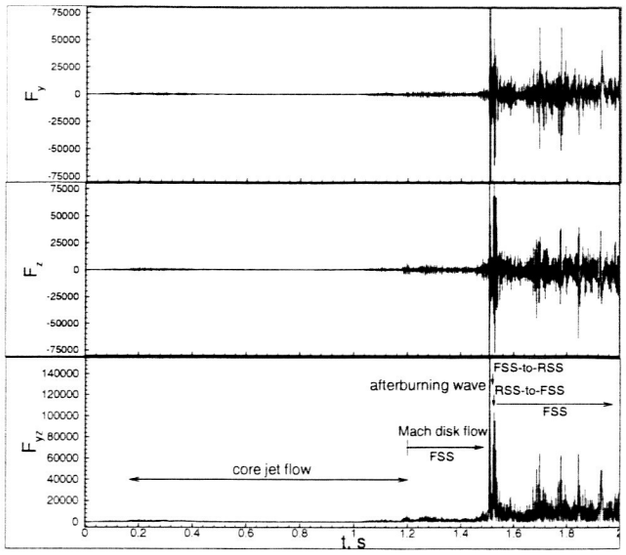

Fig. 3 Computed side forces for the adiabatic nozzle from 0 ~ 2 s.

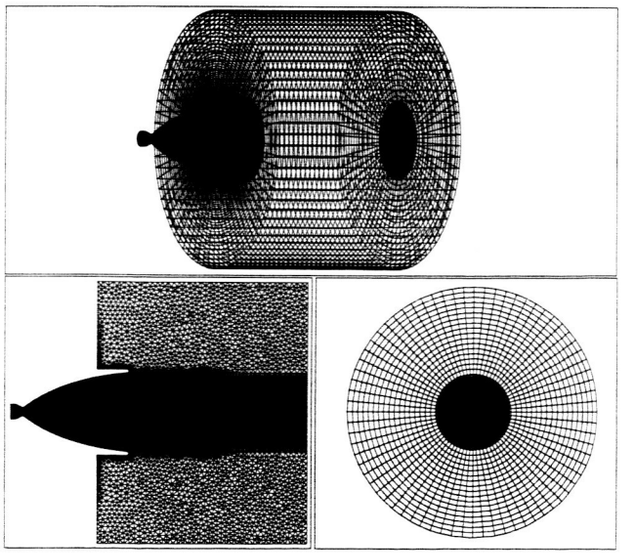

Fig. 2 The layout of hybrid grid 3d6. Top: an overall view. Bottom left: a cross-sectional cut through the nozzle axis. Bottom right: the exit plane.

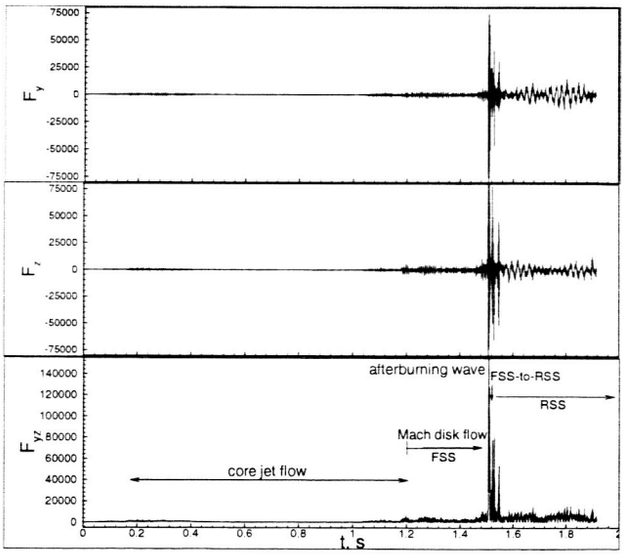

Fig. 4 Computed side forces for the cooled nozzle from 0 ~ 2 s.

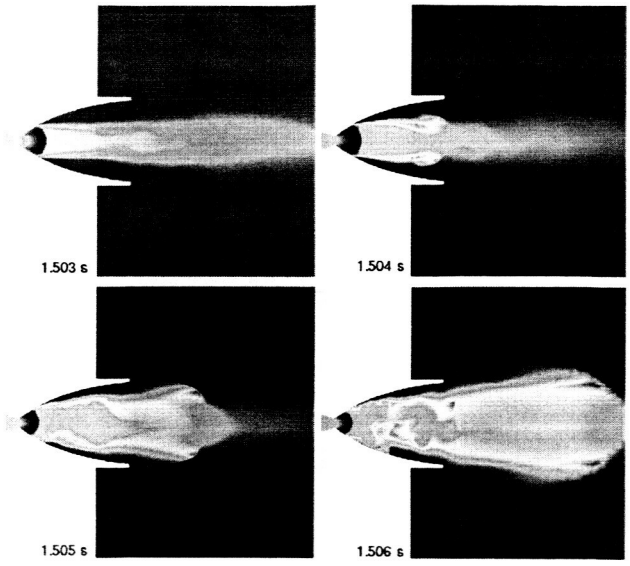

Fig. 5 Computed y-plane temperature contours of the cooled nozzle.

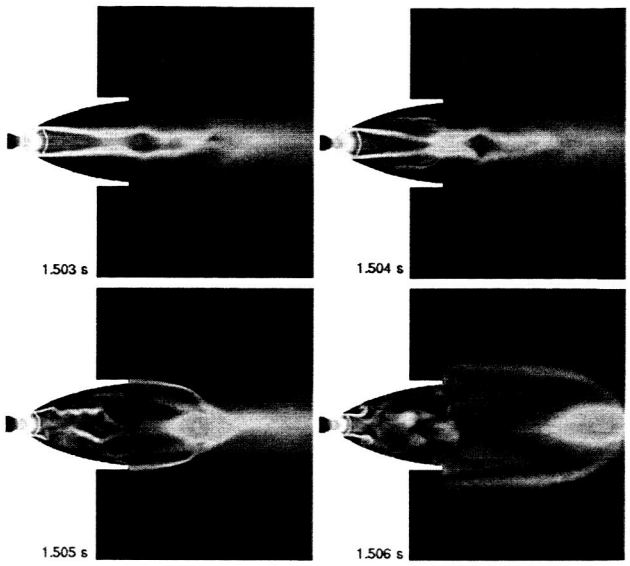

Fig. 7 Computed y-plane Mach number contours of the cooled nozzle.

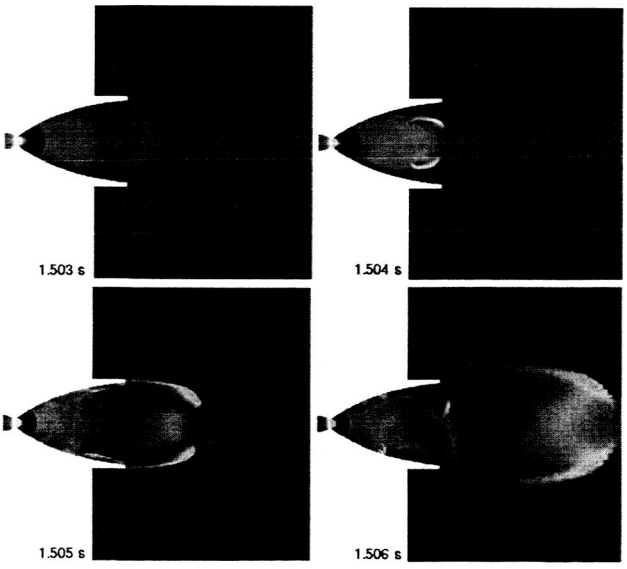

Fig. 6 Computed y-plane pressure contours of the cooled nozzle.

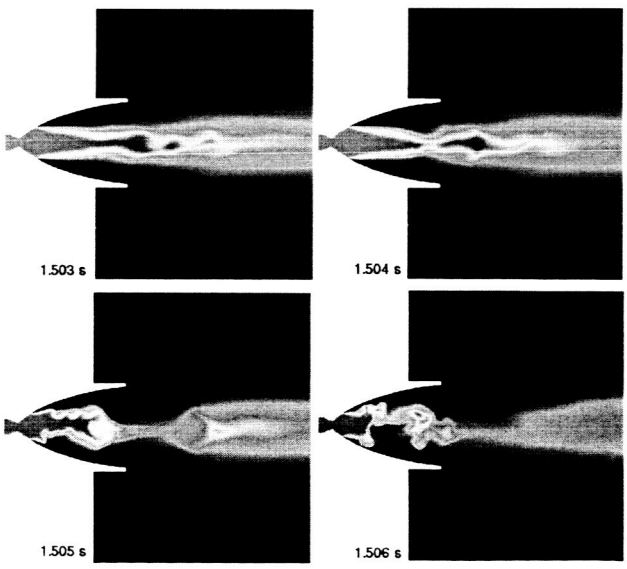

Fig. 8 Computed y-plane hydrogen mass fraction contours of the cooled nozzle.

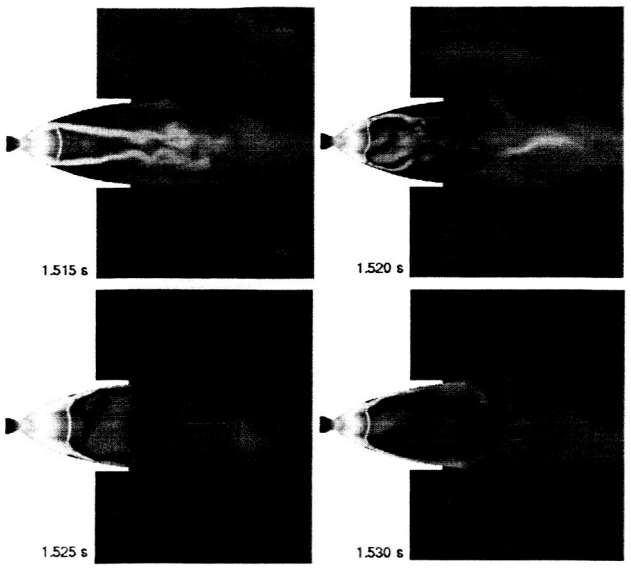

Fig. 9 Computed z-plane Mach number contours of the cooled nozzle.

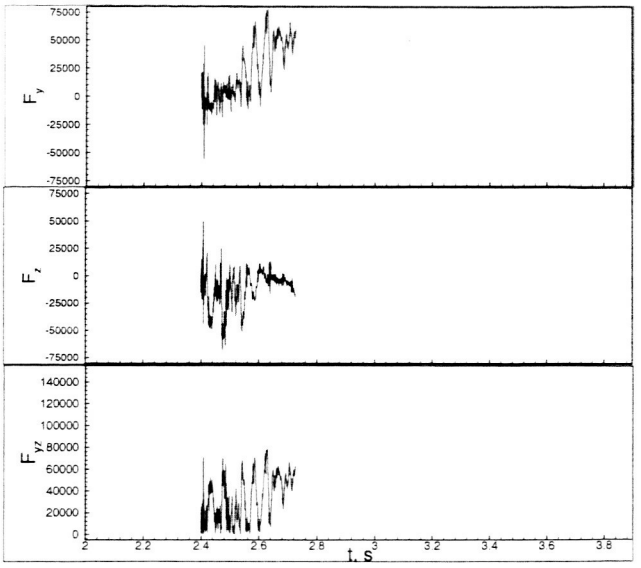

Fig. 11 Computed side forces for the adiabatic nozzle from 2 ~ 4 s.

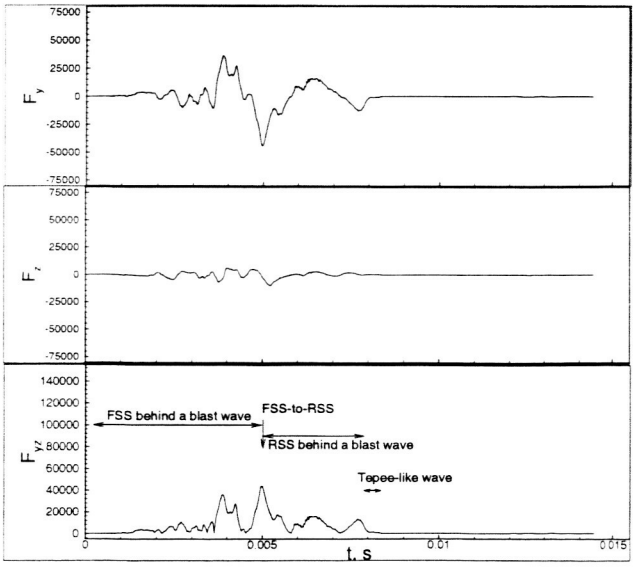

Fig. 10 Computed side forces for the adiabatic nozzle using impulse start.

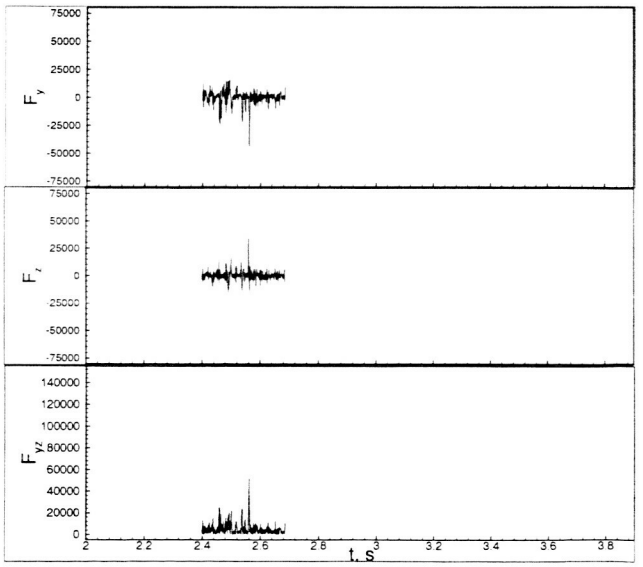

Fig. 12 Computed side forces for the cooled nozzle from 2 ~ 4 s.

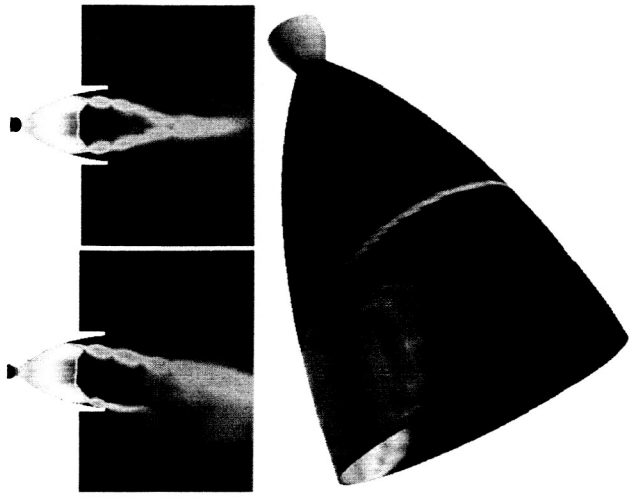

Fig. 13 Computed scalar contours for the adiabatic nozzle at 2.625 s. Top left: mach number contours on y-plane. Bottom left: Mach number contours on z-plane. Right: wall OH concentration contours.

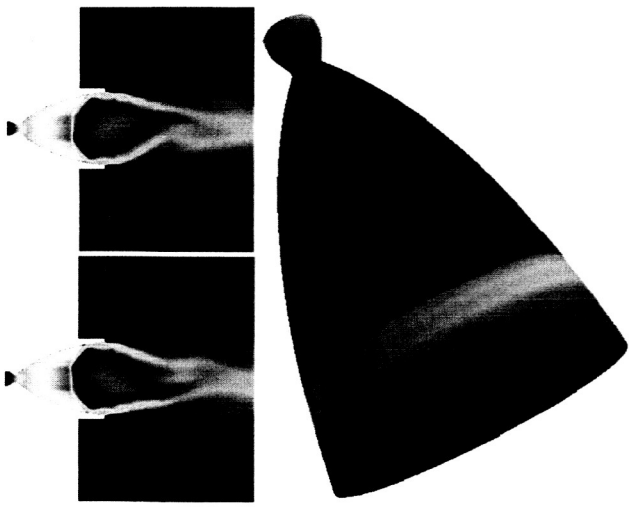

Fig. 14 Computed scalar contours for the cooled nozzle at 2.580 s. Top left: Mach number contours on y-plane. Bottom left: Mach number contours on z-plane. Right: wall OH concentration contours.

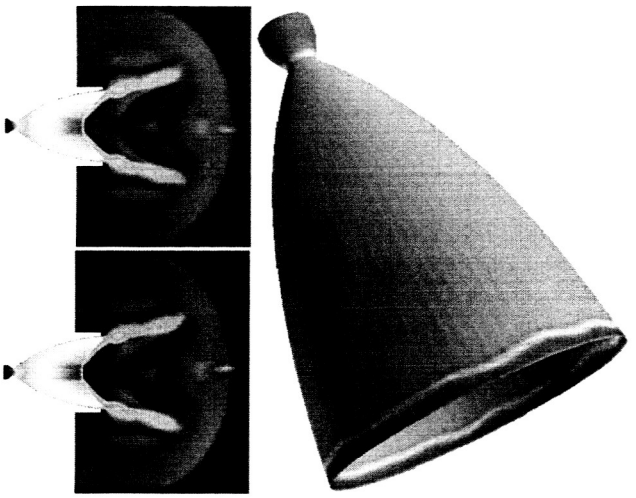

Fig. 15 Computed scalar contours for the adiabatic nozzle at 0.00825 s using impulse start. Top left: Mach number contours on y-plane. Bottom left: Mach number contours on z-plane. Right: wall OH concentration contours.